Synthesis of Ternary Nanocomposites ($SrFe_{12}O_{19}/TiO_2/ZnO$) By Sol-Gel Method for Application of Pollutant Abatement of Organic Dye Degradation Studies

Ramya Kumari Chapa*, Suneetha M., Jyothi Priya K., Sridevi Chandrakala N., Bulli Babu T., Padma M. and Sanasi Paul Douglas S.*
Department of Engineering Chemistry, Andhra University College of Engineering [A], Andra University, Visakhapatnam-530003, Andhra Pradesh, INDIA
*ramyametta99@gmail.com; spdfchem@andhrauniversity.edu.in

Abstract
The study investigates the creation of a ternary metal oxide nanocomposite ($SrFe_{12}O_{19}/TiO_2/ZnO$) designed to be an effective and superior photocatalyst. This is concluded by sequentially embedding semiconductors onto an n-type semiconductor using chemical or sol-gel methods. The formational and consistency properties of the resulting sample were analyzed using a range of methods involving X-ray diffraction (XRD), Fourier-transform infrared (FTIR) spectroscopy, Field emission scanning electron microscopy with Energy-dispersive spectroscopy (FESEM-EDS), UV-visible spectroscopy, Transmission electron microscopy (TEM) and Vibrating sample magnetometry (VSM). The photocatalytic activity of the ternary nanocomposite was evaluated by testing its effectiveness in degrading Methylene Blue and Rhodamine B dyes under visible light.

Under sunlight, methylene blue and rhodamine B were completely degraded by the nanocomposite in 60 and 50 minutes respectively. The main reactive species responsible for the photodegradation under visible light were hydroxyl radicals (•OH) and superoxide anions ($•O_2^-$). Additionally, the small particle size, high catalytic efficiency and favorable *physical and chemical properties of the $SrFe_{12}O_{19}/ZnO/TiO_2$ nanocomposites contributed to their excellent reusability.*

Keywords: $SrFe_{12}O_{19}/ZnO/TiO_2$ nanomagnetic composites, Sol-gel method, Visible-light Photodegradation, Methylene blue and Rhodamine-B dye.

Introduction

As economic development and population growth continue, the protection of water resources is becoming more crucial, especially given that around two million tons of garbage contaminants are irresponsibly dumped into tap water supplies daily, which severely impacts public health and leads to numerous fatalities[7]. The majority of chemical contaminants that are soluble in water, are bad for the environment for people. Over 35% of deaths in poor countries are linked to problems with water and an estimated 1.1 billion people do not have access to clean water[12]. The most typical contaminants include monoaromatic hydrocarbons, residual poisonous dyes and industrial waste-derived antibiotics such as naproxen (NPX), 4-nitrophenol (4-NP) and rhodamine B (Rh B), which are stable against heat and light[7].

Rhodamine B ($C_{28}H_{31}N_2O_3Cl$) is a widely used tracing material and anthemic dye known for its cationic properties, allowing it to dissolve both organic solvents and water, making it extensively utilized in the textile industry [9]. Both humans and animals are at risk from Rh B exposure. Acute symptoms include burning in the eyes, excessive tears, burning and itching in the nose, chest pain, burning in the throat, rhinorrhea, coughing, headaches and nausea[15]. Photocatalysis breaks down organic pollutants in wastewater into water, carbon dioxide, or other tiny molecules while reducing or oxidizing inorganic toxins into safe chemicals under mild conditions using green technology and a straightforward method. Nevertheless, deactivated photocatalysts are prone to self-etching and intrinsically unstable[6].

The metal-replaced, co-doped nanomaterial is employed as a degradation process photocatalyst. The application of dopant ferrites, which effectively reduces the band gap and facilitates absorption, is highly beneficial for the process of photocatalytic degradation[14]. Strontium ferrite is highly regarded for its exceptional corrosion and heat resistance and its usefulness in various applications, with its strong magnetic anisotropy and high coercivity due to its crystalline structure, recently attracting significant attention from researchers[11]. Due to their commercial applications, hexagonal ferrites $MFe_{12}O_{19}$ (where M = Ba, Sr and Pb) have long piqued the interest of researchers. Strontium hexaferrite is especially appreciated for its hard magnetic characteristics.

Due to their magnetic characteristics, these ferrites are considered ideal materials for higher-frequency devices, electric motors, toys, microwave components, permanent magnets, loudspeakers and perpendicular magnetic recording media[3]. The accumulation that results from the magnetic dipole interaction between ferrite particles affects the fabrication of $SrFe_{12}O_{19}$[4]. M-type $SrFe_{12}O_{19}$, with an Eg value of around 2.92 eV, is an eco-friendly magnetic n-type semiconductor that effectively degrades various synthetic

organic dyes including methyl orange, toluidine blue and MB. It also boasts notable attributes such as chemical stability, cost-effectiveness and permanent magnetism, which make it useful for magnetic hyperthermia, microwave absorption, corrosion resistance and recording media.

$SrFe_{12}O_{19}$'s primary benefits as a photocatalyst are its reusability and ease of recovery, magnetic characteristics, ease of separating using an external magnetic field and stopping more pollution from entering the treated solution[16]. Due to its suitable magnetic characteristics, chemical stability and reasonable price in comparison to rare-earth compounds, it has attracted significant attention in recent years[18]. A strontium ferrite ($SrFe_{12}O_{19}$) based ferromagnetic catalyst (TiO_2) has strong magnetic characteristics.

The recovery and reuse are simple processes. The additional catalyst increases visible light absorption, which increases its activity when spilled into sunshine[1]. In actuality, a composite of magnetic/titania can be made and an external magnetic field can be applied to control and collect photocatalysts. However, due to photo-dissolution effects, titania's photocatalytic activity may decrease when it comes into direct contact with the magnetic cores[5].

One of the applications of heavy metal ions that has been investigated most, is the medicinal use of Cr (VI) ions. The photocatalytic reduction of Cr (VI) with catalysts based on TiO_2, ZnO, CdS and ZnS has been the subject of several published investigations[17]. Among the several metal oxide semiconductors, zinc oxide (ZnO) has attracted a lot of interest from academics and entrepreneurs because of its potent oxidation ability, advantageous photoelectric and catalytic qualities, chemical resistance, lack of toxicity and affordable price. ZnO nanoparticles (NPs) are n-type group II-VI semiconductors with a wide bandgap of 3.37 eV and many active photodegradation sites.

However, ZnO's photocatalytic efficacy is limited to the UV area due to its broad bandgap, which only allows it to interact with UV light at wavelengths lower than 387 nm[8].

All three of the TiO2 polymorphs: rutile (tetragonal), brookite (orthorhombic) and anatase (tetragonal), are n-type semiconductors that are non-toxic. Anatase is thought to have a metastable phase at lower temperatures and is challenging to synthesize because of its propensity for phase transition. Despite this, its 3.2 eV bandgap energy allows it to display amazing chemical and physical features[10]. The sol-gel method provides for the creation of remarkably pure composites with a 99.99% homogeneity. This is a wet chemical process that works very well for creating many kinds of nanostructures, like metal oxide nanoparticles[2].

Material and Methods

The chemicals utilized in this work included zinc nitrate, ethylene glycol, Strontium nitrate, ferric citrate, citric acid, titanium tetra chloride and hydrochloric acid.

Chemical compound	Chemical composition	Make
Zinc nitrate	$Zn(NO_3)_2$	Chemie
Titanium Chloride	$TiCl_4$	Loba Chemie
Strontium Nitrate	$Sr(NO_3)_2$	Reachem
Ferric citrate	$C_6H_5FeO_7$	Sisco
Citric acid	$C_6H_8O_7$	Loba Chemie
Copper nitrate	$Cu(NO_3)_2$	Loba Chemie
Hydro chloric acid	HCl	Moly Chem
Ammonium Hydroxide	NH_4OH	Ran keen
Ethylene glycol	$C_2H_6O_2$	Sisco

Synthesis of Strontium ferrite: To prepare the ferric citrate solution, 4.23 g of strontium nitrate is dissolved in 10 mL of distilled water in a single beaker, fill another beaker with 71.64 g of ferric citrate and 10 mL of water. Add 12.6 g of citric acid to the liquids in beakers 1 and 2. Adding ammonia gradually will keep the solution at pH [neutral]. Add 20 mL of ethylene glycol to the mixture, then use a hot plate to create a dry powder. After two hours of calcination at 800^0C, the finely powdered nano strontium ferrite has evolved.

Synthesis of Titania Nano Composites: A white precipitate formed as 6.9 mL of $TiCl_4$ was gradually added to a beaker containing 350 mL of distilled water and 0.5 mL HCl solution. The beaker was covered with aluminum foil to protect the reaction from light. After forming the precipitate, the mixture was agitated for one hour. It was then heated on a hot plate at a temperature range of 80-100^0C with continuous stirring. This process resulted in the formation of a fine nano titania powder [13]

Synthesis of Zinc Oxide Nano Composites: A mixture of 20 mL of ethylene glycol and 5 grams of zinc nitrate was stirred for an hour. When a homogeneous solution was obtained, it was kept at room temperature for one day. The mixture was formed into a gel. The solution was then heated on a hot plate, crushed and dried. Finally, the material was calcined at 500^0C for two hours. The finely powdered nano zinc oxide has evolved.

Synthesis of $SrFe_{12}O_{19}/TiO_2/ZnO$ ternary nano-composites: Ternary nanocomposites were synthesized by combining 0.8, 0.1 and 0.1 grams respectively. Specifically, 0.8 g of $SrFe_{12}O_{19}$, 0.1 g of TiO_2 and 0.1 g of ZnO were accurately weighed and thoroughly mixed using a mortar and pestle to form a homogenous powder.

Instrumentation: The resulting materials were studied in the 500–4000 cm^{-1} range by Infrared spectroscopy using the IR Prestige 21. With a diffractometer, the X-ray diffraction (XRD) pattern was produced. In the angular range of 10-80 *(2 theta), samples from the Bruker DX-5 were scanned. The UV–DRS spectra were obtained with Shimadzu 2600R barium sulfate as a reference in the 500–4000 cm^{-1} range. Using a Zeiss Germany 300 Scanning electron microscope, morphology and microstructure were investigated.

Results and Discussion

UV-DRS: The magnetic material $SrFe_{12}O_{19}/TiO_2/ZnO$ nanocomposite was estimated by using UV diffuse reflectance spectroscopy as shown in the figure. Nano strontium ferrite exhibits a lambda maximum at 365 nm with a calculated bandgap of 3.3 eV. In contrast, the $SrFe_{12}O_{19}/TiO_2/ZnO$ nanocomposite indicates a lambda maximum at 351 nm, with the calculated bandgap reduced to 2.3 eV. I.e. In comparison to a single strontium ferrite, the nanocomposite's bandgap has significantly decreased, suggesting increased absorption in the visible light spectrum.

.

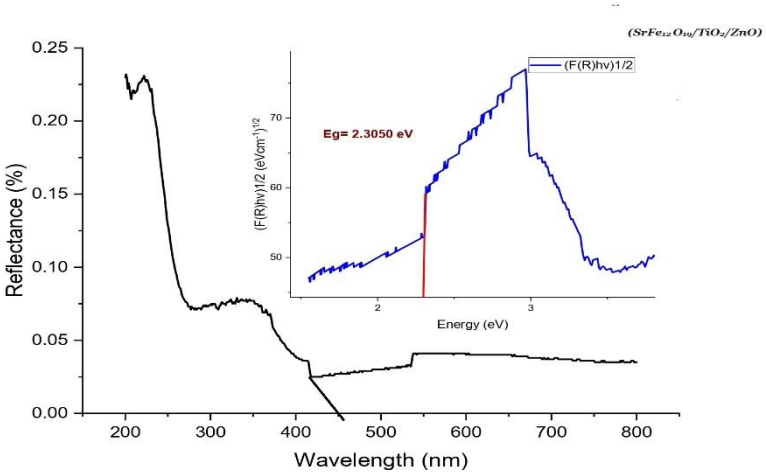

Fig. 1: UV-Visible diffuse reflectance spectra $SrFe_{12}O_{19}/TIO_2/ZnO$

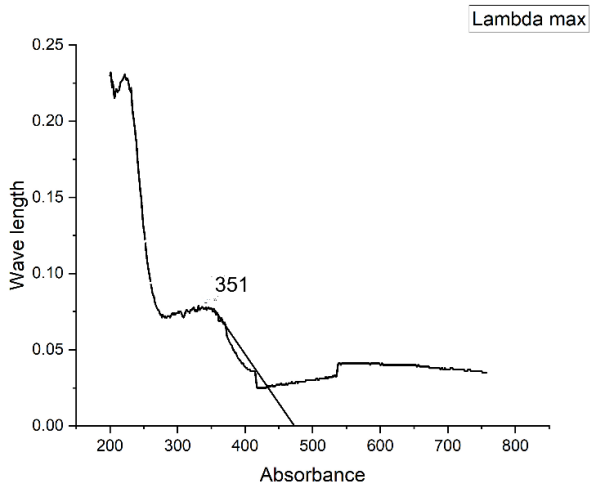

Fig. 2: Band gap of $SrFe_{12}O_{19}/TiO_2/ZnO$

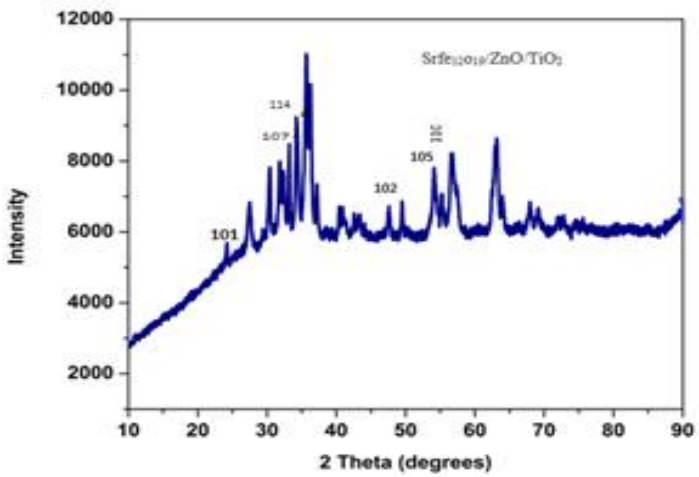

Fig. 3: XRD pattern of $SrFe_{12}O_{19}/TiO_2/ZnO$

XRD: The X-ray diffraction (XRD) patterns for $SrFe_{12}O_{19}$ powder and the $SrFe_{12}O_{19}/ZnO/TiO_2$ photocatalytic composite are presented in the figure. The diffraction peaks correspond to JCPDS Card No. 79-1411 and are consistent with the $SrFe_{12}O_{19}$ phase, the anatase TiO_2 phase (JCPDS Card Nos. 21-1272 and 21-1276) and ZnO (JCPDS Card No. 36-1451). The observed 2θ values are 25°, 28°, 29°, 30°, 31°, 32°, 35°, 42°, 45°, 49°, 50°, 55°, 58°, 60°, 65°, 69° and 70°. Specifically, the 2θ peaks at 34°, 35°, 56° and 57°, corresponding to the planes (107), (114) and (2011), indicate the presence of strontium ferrite.

Additionally, the 2θ peaks at 49° and 56°, corresponding to the planes (102) and (110), confirm the presence of ZnO, while the 2θ peaks at 25° and 55°, corresponding to the planes (101) and (105), signify the presence of titanium. The diffractograms exhibit intense peaks, demonstrating the crystallinity of the samples. Therefore, the XRD pattern confirms the formation of the $SrFe_{12}O_{19}/TiO_2/ZnO$ spinel ferrite composite.

SEM images and EDX analysis: The sizes and morphologies of the resultant $SrFe_{12}O_{19}/TiO_2/ZnO$ ternary nanocomposites were examined using Scanning electron microscopy (SEM). The SEM images demonstrate that the diameter range of the $SrFe_{12}O_{19}/TiO_2/ZnO$ nanoparticles is 18–50 nm. The morphologies and sizes of the synthesized $SrFe_{12}O_{19}/TiO_2/ZnO$ ternary nanocomposites were examined using Scanning electron microscopy (SEM). The SEM images reveal that the $SrFe_{12}O_{19}/TiO_2/ZnO$ nanoparticles have diameters ranging from 18 to 50 nm. Pure ZnO nanoparticles, observed in the images, are relatively large due to the agglomeration of primary particles and exhibit disc-like and spherical shapes with relatively smooth surfaces.

Energy-dispersive spectroscopy (EDS) analysis, as depicted, confirms that these ZnO nanoparticles consist solely of zinc and oxygen elements. The SEM micrographs of the $SrFe_{12}O_{19}/TiO_2/ZnO$ nanocomposites show particles with spherical and sheet-like morphologies and rough surfaces. The EDS analysis of these nanocomposites, shown in the figures and the figure insets, reveals the presence of zinc, oxygen, titanium, strontium and iron elements. These morphological observations and EDS results are consistent with the X-ray diffraction (XRD) data, which validate the purity of the fabricated ternary nanocomposite structure.

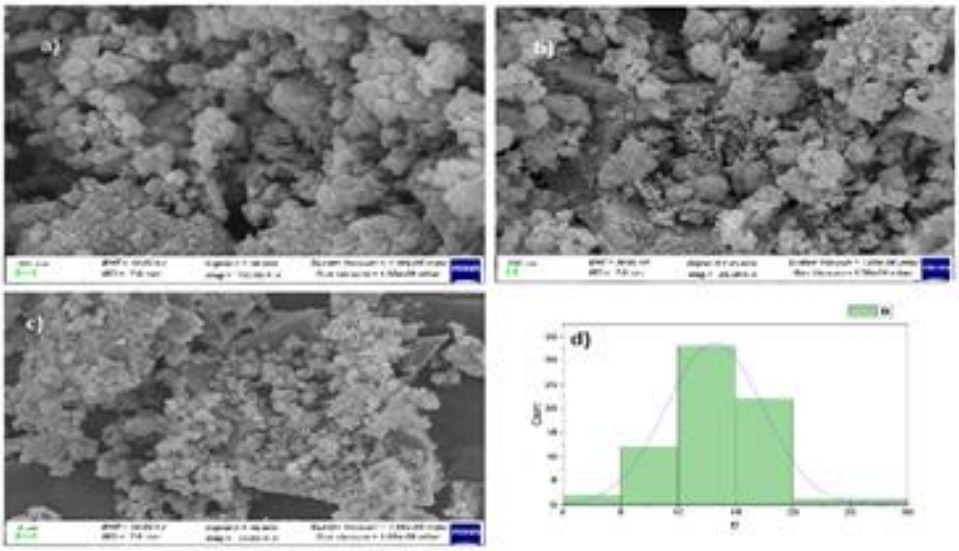

Fig. 4: SEM images of $SrFe_{12}O_{19}/TiO_2/ZnO$ (a) 100 nm (b) 200 nm (c) 1µm (d) particle size distribution of SrFe12O19/TiO2/ZnO

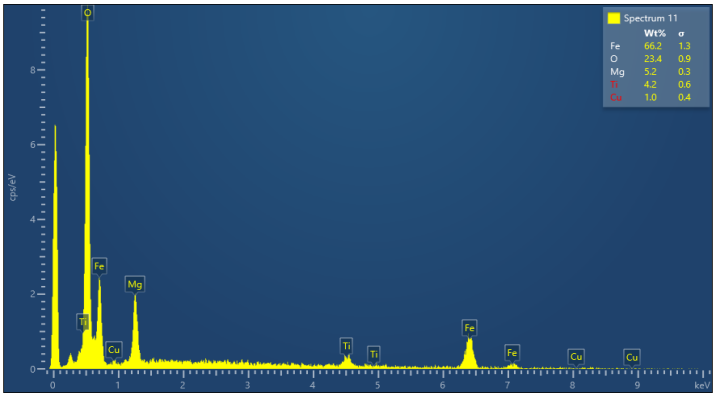

Fig. 5: EDX spectrum of $SrFe_{12}O_{19}/TiO_2/ZnO$

Element	Wt.%	Atomic %
O	30.97	61.53
Ti	20.79	13.80
Fe	17.09	9.72
Zn	29.57	14.38
Sr	1.58	0.57
Total	100.00	100.00

TEM: The TEM images were appropriate for inspecting the structure and characteristics of the produced materials. The figure displays a TEM micrograph of the $SrFe_{12}O_{19}/TiO_2/ZnO$ nanoparticles, which have an average diameter of 30 nm. The TEM image reveals that these nanoparticles are relatively rough and spherical. The TEM micrograph of $SrFe_{12}O_{19}/TiO_2/ZnO$, as shown in the figure, exhibits a similar morphology to the previous image, with the additional observation of a ZnO layer situated between the $SrFe_{12}O_{19}$ and TiO_2, as highlighted in the figure. These findings align with reports in the literature, validating the successful combination of the nanoparticles and photocatalyst composites.

Additionally, the figure includes a TEM image of the TiO_2 photocatalyst, showing the synthesized structure. Following the findings of the XRD examination, the TiO_2 photocatalyst was primarily composed of elementary particles with sizes ranging from 15 to 26 nm. The majority of the elementary particles in the TiO_2 photocatalyst ranged in size from 15 to 26 nm, which is in line with the findings of the XRD study.

FTIR: Fourier transform infrared (FTIR) spectroscopy was used to further analyze the $SrFe_{12}O_{19}$ powder and the synthesized photocatalytic composites. In the FTIR spectrum of $SrFe_{12}O_{19}$, peaks within the range of 450–493 cm^{-1} correspond to the natural vibrations of the tetrahedral and octahedral sites in its structure. A peak at 3418 cm^{-1} is associated with the O–H bending vibration of chemically adsorbed water and the O–H stretching mode of free water molecules on the surface.

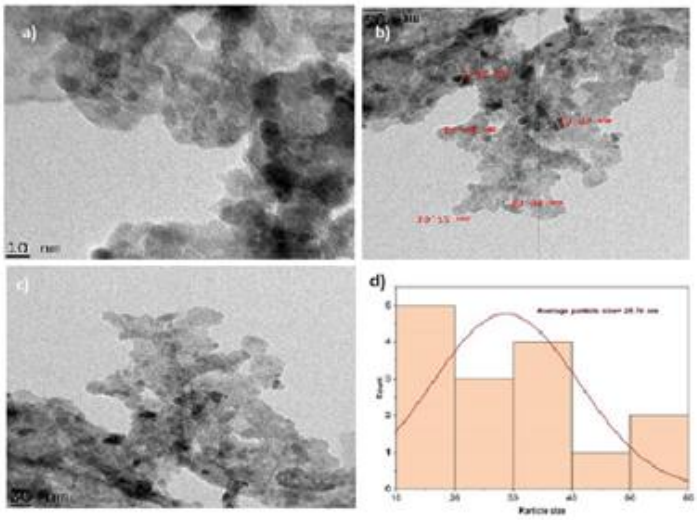

Fig. 6: TEM images of $SrFe_{12}O_{19}/TiO_2/ZnO$ (a) 10 nm (b) 20 nm (c) 50 nm (d) particle size distribution of $SrFe_{12}O_{19}/TiO_2/ZnO$ (TEM)

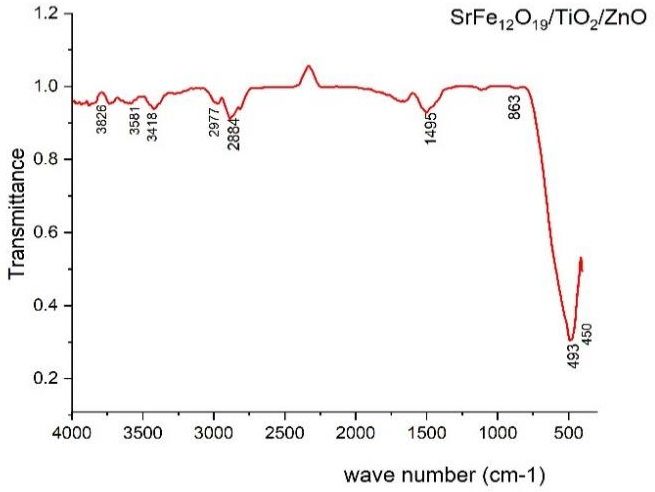

Fig. 7: FTIR of $SrFe_{12}O_{19}/TiO_2/ZnO$

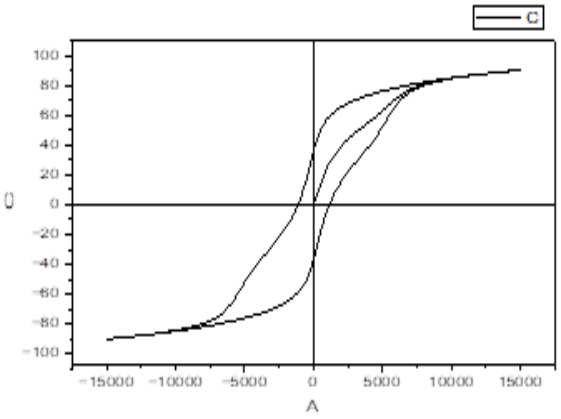

Fig. 8: Magnetization loop for $SrFe_{12}O_{19}/ZnO/TiO_2$ composite at room temperature

In the $SrFe_{12}O_{19}/ZnO/TiO_2$ composite, the observed shift to lower frequencies, along with increased broadening and intensity of these bands, indicates a higher concentration of surface hydroxyl groups. These surface hydroxyl groups are known to act as active sites for adsorption, hydroxyl radical generation and oxidative decomposition, implying that the $SrFe_{12}O_{19}/ZnO/TiO_2$ composite may possess enhanced catalytic activity for pollutant removal. The $SrFe_{12}O_{19}/ZnO$ composite shows an absorption peak of around 450 cm^{-1}, attributed to asymmetric stretching vibrations. Asymmetric Ti–O–Zn vibration is observed at 493 cm^{-1}, suggesting the formation of a covalent bond between TiO_2 and ZnO. This bond may enhance the adhesion of TiO_2 to the surface of the $SrFe_{12}O_{19}/ZnO$ composite. Additionally, a peak at 800 cm^{-1} corresponds to the absorption band of Ti–O–Ti, indicating a four-fold coordination.

Magnetic Properties: At room temperature, we utilized VSM to examine the magnetic properties of the material. The magnetic characteristics of the synthesized nanocomposite are a key feature of a reusable and regenerable magnetic heterogeneous catalyst. The $SrFe_{12}O_{19}/TiO_2/ZnO$ composite displays superparamagnetic behavior, with a saturation magnetization of 82 emu/g and near-zero coercivity. Similarly, magnesium ferrite nanoparticles also exhibit superparamagnetic properties. The presence of metal oxides in the composite results in reduced magnetization. This nanocomposite is well-suited for applications involving the reusable magnetic separation of photocatalytic particles, making it beneficial for minimizing secondary pollution in water treatment processes. The figure shows the magnetic hysteresis curve.

Evaluation of Photocatalytic efficiency of catalyst by degradation of Methylene blue dye and Rhodamine B: The effectiveness of the catalyst in degrading methylene blue and rhodamine B dyes is assessed through photocatalysis. The impact of different reaction parameters including irradiation, temperature, pH, catalyst dose and initial dye concentrations, was investigated to determine the optimal conditions for improving the photocatalytic degradation of MB and Rh-B**.** This involved adjusting one parameter at a time while keeping the others constant.

Impact of the initial dye concentration: The initial dye concentration significantly impacts the photocatalytic degradation of MB and RhB by the $SrFe_{12}O_{19}/TiO_2/ZnO$ composite. For this study, an optimal pH of 6 and 8 and a photocatalyst dosage of 0.4 g/L for both MB and RhB were used. As shown in the figures, the photodegradation efficiency decreases as the initial dye concentration increases. Regardless of the dye type, the highest and lowest levels of dye removal are observed at initial concentrations between 5 and 100 mg/L. The photocatalytic degradation efficiency is 100% visible at 130 min in MB and 140 min in RhB. Prolonging the interaction between dye molecules and the photocatalyst enhances removal efficiency by increasing the density of active sites, resulting in higher production of H+ and OH ions.

The greater concentration of hydroxyl radicals and more efficient activation of photocatalyst nanoparticles under visible light leads to higher photodegradation efficiency at lower dye concentrations. In contrast, the reduced efficiency at higher concentrations is due to light absorption by the dye molecules, which prevents photons from reaching the photocatalyst surface.

Effect of pH: A pH range of 5-8 was used to examine the photodegradation efficiency of $SrFe_{12}O_{19}/TiO_2/ZnO$ photocatalysts. A photocatalyst dose of 0.40 g/L and a dye concentration of 10 mg/L were consumed for both MB and RhB. The maximum efficiency was noted at pH 6 for methylene blue and pH 8 for rhodamine b, as indicated in figure. Methylene blue was visible for 100 minutes and 80 minutes to visible light respectively. For both MB and RhB, the dye's degradation efficiency was 100%. Overall, the data indicate that photodegradation efficiency generally increases at pH-6 and pH-8 concentrations**.**

Effect of Temperature: A temperature range of 25°C to 40°C was used to study the impact of temperature on the nanocomposites' ability to adsorb MB and RhB dyes. The variation in uptake percentages over time at various temperatures is depicted in the figure. Maximum efficiency was achieved in the adsorption of MB and Rh-B when the temperature rose from 35°C to 40°C. Throughout the

investigation, dye solution concentrations were kept at 10 ppm respectively. Both dyes had the maximum adsorption capacity and efficiency (100%) when broken down at 40°C for 90 minutes for MB and 70 minutes for RhB. These results imply that the adsorption process is endothermic since MB and RhB are better able to bind to the adsorbent at higher temperatures. The higher temperature allows more dye to penetrate the adsorbent.

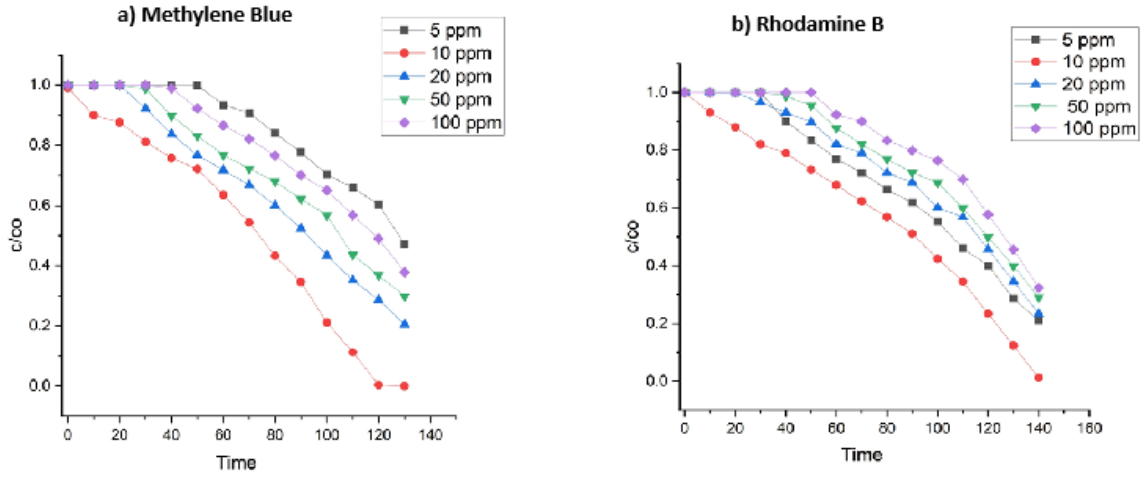

Fig. 9: Effect of initial dye concentration on photocatalytic degradation of a) Methylene Blue b) Rhodamine B

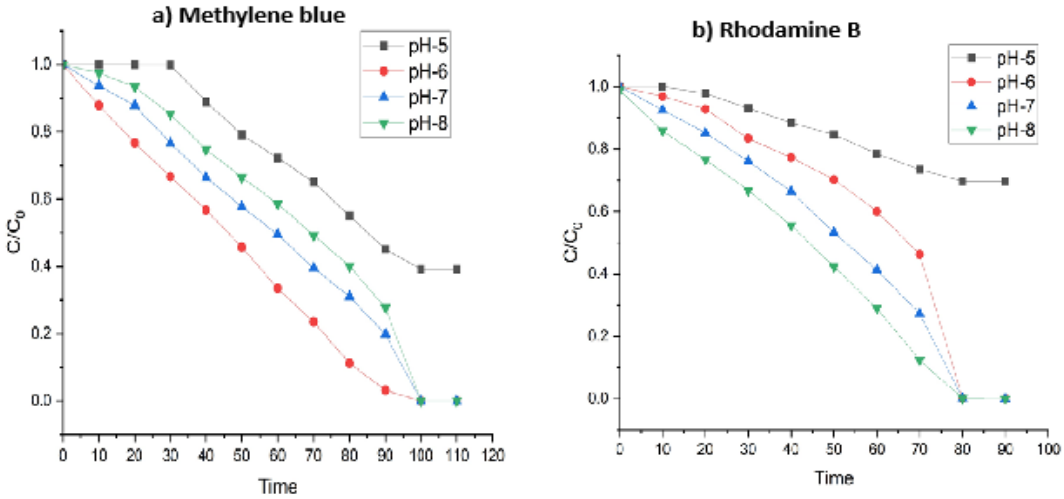

Fig. 10: Effect of pH on photocatalytic degradation of a) Methylene Blue b) Rhodamine B

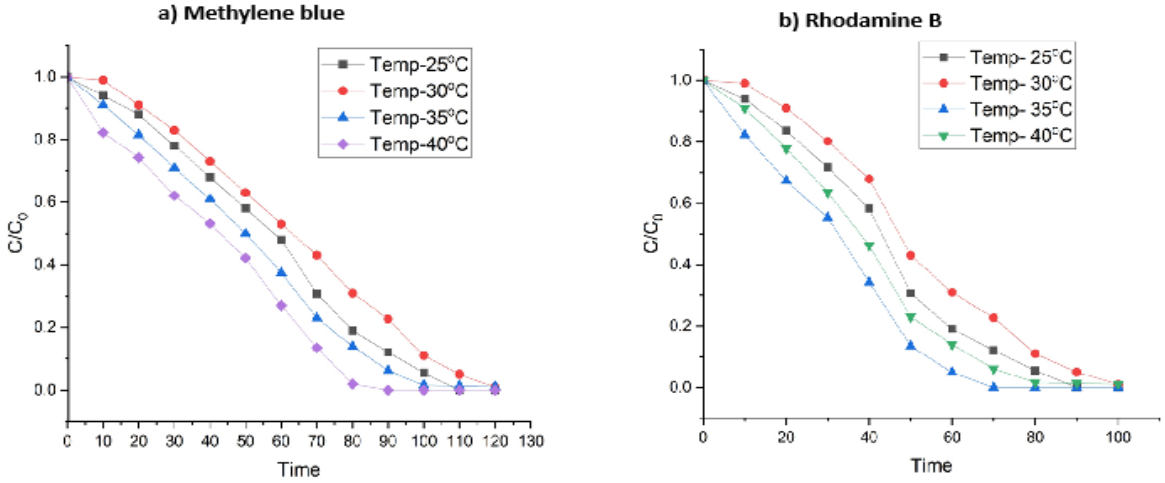

Fig. 11: Effect of temperature on photocatalytic degradation of a) Methylene Blue b) Rhodamine B

Effect of Catalyst dosage; Impact of varying photocatalyst dosages (0.25, 0.35, 0.45 and 0.55 g/L) on the photodegradation of MB and RhB dye models was studied. As illustrated in the figure, photodegradation efficiency increases with the photocatalyst dosage up to a threshold of 0.45 g/L for both dyes for MB at 60min and Rh B at 50min. At this dosage, the higher density of photocatalyst particles produces a proportional rise in reactive sites, which enhances dye molecule interaction, adsorption and the production of OH radicals. However, exceeding this dosage leads to a decline in photodegradation efficiency, likely due to particle aggregation, which hinders light penetration and reduces dye exposure on the photocatalyst surface.

Effect of Irridation: The absorption spectra of MB and Rh B dyes were monitored during solar photocatalysis using $SrFe_{12}O_{19}/TiO_2/ZnO$ catalysts. Over time, the absorption peaks at 565 nm for rhodamine B and 662 nm for methylene blue gradually decreased. The efficiency of the catalysts under study was plotted as C/C0 versus time, as shown in the figures. After 60 minutes, the $SrFe_{12}O_{19}/TiO_2/ZnO$ photocatalysts achieved a maximum MB degradation of 100% and Rh B at 50min achieving their superior photocatalytic activity. In contrast, when MB dye was exposed to sunlight without a catalyst, it degraded by maximum highlighting the effectiveness of the developed photocatalyst activity.

Stability and Reusability: The stability and reusability of a photocatalyst are fundamental for its functional use. To evaluate these aspects, following each degradation cycle, the photocatalyst was recovered, rinsed with methanol and water and vacuum-dried for 24 hours at 90°C. Fresh degradation tests were then performed using the recycled catalyst under optimal conditions. After three cycles, the photodegradation efficiency decreased to 85 % for MB and 79 % for RhB, as shown in the figure 14.

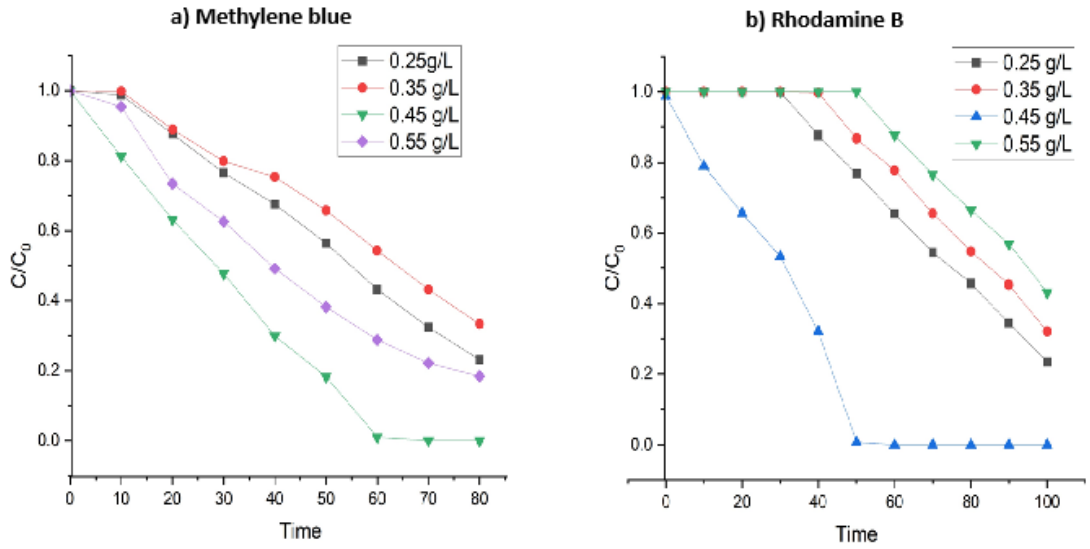

Fig. 12: Effect of catalyst dosage on photocatalytic degradation of a) Methylene Blue b) Rhodamine B

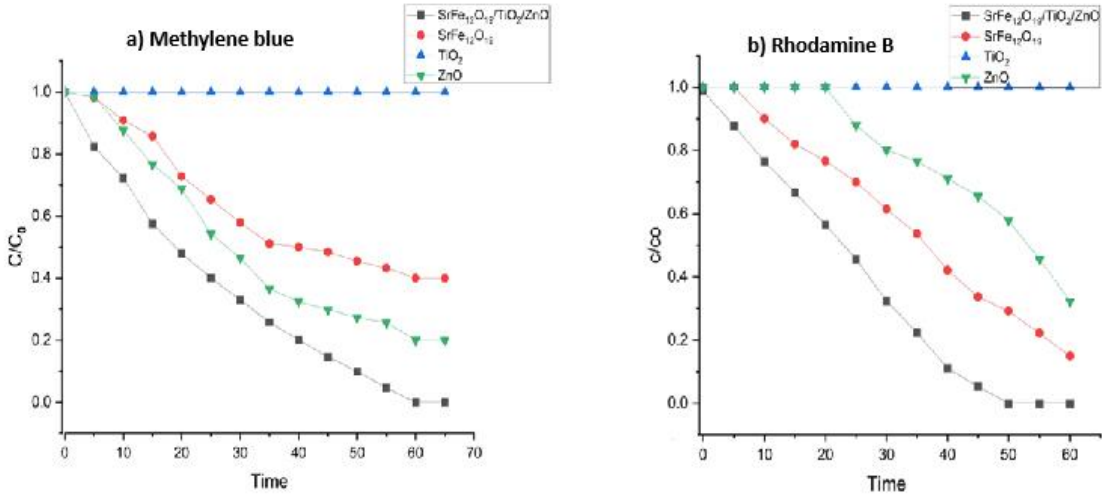

Fig. 13: Effect of irradiation time on photocatalytic degradation of a) Methylene Blue b) Rhodamine B

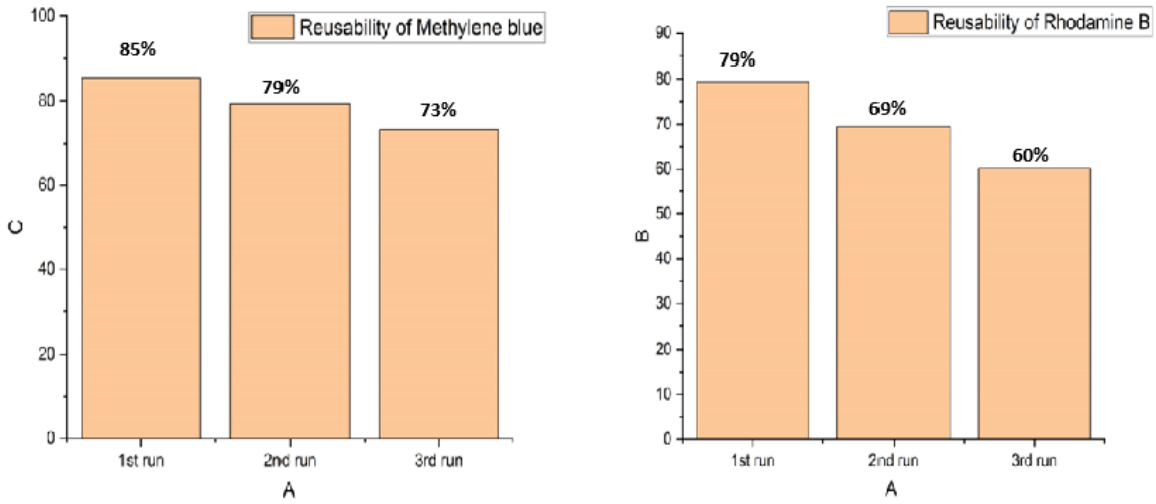

Fig. 14: Reusability of a) Methylene Blue b) Rhodamine B

Table 1
Results of Antibacterial activity by prepared $SrFe_{12}O_{19}/TiO_2/ZnO$

Sample Number	Sample	Concentration {µg/mL}	*Staphylococcus aureus* {Gram-positive} (mm)	*Escherichia Coli* {Gram-negative} (mm)
A)	$SrFe_{12}O_{19}/TiO_2/ZnO$ synthesized	20	2	3
		80	2	3
		150	2	4
	Amikacin	10	13	15
B)	$SrFe_{12}O_{19}/TiO_2/ZnO$	20	4	5
	Nanocomposite	80	5	8
		150	9	11
	Amikacin	10	14	15

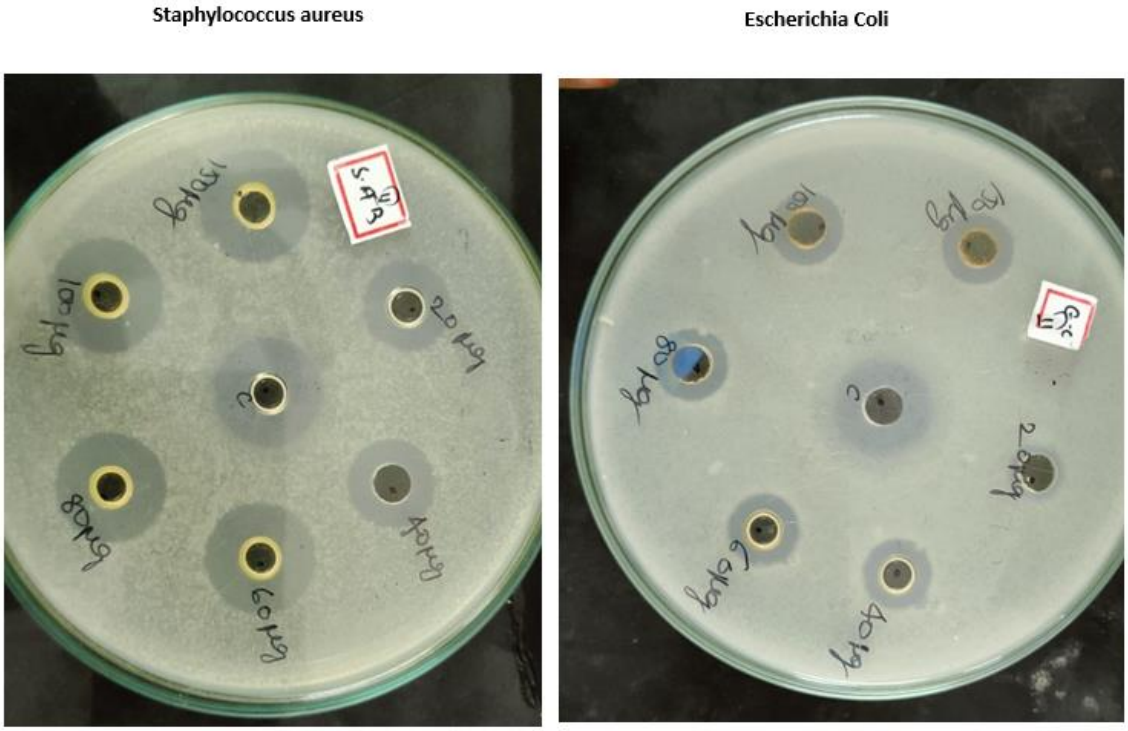

Antibacterial Activity: The antibacterial activity of the as-synthesized $SrFe_{12}O_{19}/TiO_2/ZnO$ materials and the $SrFe_{12}O_{19}/TiO_2/ZnO$ nanocomposite was examined using the disc diffusion method. Using Amikacin as a reference, the activity was examined against *Staphylococcus aureus* and *Escherichia coli*. The manufactured materials were spread out on plates containing bacteria after being sonicated in distilled water. The inhibition zones were visible on these plates following a day of incubation. The presence of these zones of inhibition verified the antibacterial properties of the produced samples.

Compared to $SrFe_{12}O_{19}/TiO_2/ZnO$, the nanocomposite exhibits greater antibacterial action against *S. aureus* and *Escherichia coli*. Table 1 demonstrates that the activities increased as the sample concentration arose. The inhibition zone's considerable size indicates strong antibacterial activity. Therefore, the $SrFe_{12}O_{19}/TiO_2/ZnO$ nanocomposite is a potent antibiotic that works against *S. aureus* and *E. coli*.

Conclusion

This work presents the nanocomposite magnetic photocatalyst. The $SrFe_{12}O_{19}/TiO_2/ZnO$ nanocomposite was synthesized using the Sol-gel method. Its photocatalytic activity was tested using methylene blue and rhodamine B under UV visible light irridation. The characterization results obtained through UV-DRS, XRD, SEM, TEM, FTIR and VSM indicate that $SrFe_{12}O_{19}/TiO_2/ZnO$ is a good photocatalytic, recyclable and reduced nanocomposite.

Acknowledgement

The authors express their gratitude to Andhra University Advanced Analytical Laboratory for providing them with spectral analysis.

References

1. Azrina Abd Aziz, Gianluca Li Puma, Shaliza Ibrahim and Pichiah Saravanan, Preparation, characterization and solar photoactivity of titania-supported strontium ferrite nanocomposite photocatalyst, *Journal of Experimental Nanoscience,* **8(3)**, 295 https://doi.org/10.1080/17458080.2012.675087 **(2013)**

2. Dmitry Bokov, Abduladheem Turki Jalil, Supat Chupradit, Wanich Suksatan, Mohammad Javed Ansari, Iman H. Shewael, Gabdrakhman H. Valiev and Ehsan Kianfar, Nanomaterial by Sol-Gel Method: Synthesis and Application, *Advances in Materials Science and Engineering*, https:\doi.org\10.1155\2021\5102014 **(2021)**

3. Ehsan Naderi, Mahmoud Naseri and Dariush Souri, The effect of SiO_2 and TiO_2 nanoparticles on physical properties of $SrFe_{12}O_{19}$ nanoparticle, *Current Applied Physics*, **18**, 469, https://doi.org/10.1016/j.cap.2018.01.008 **(2018)**

4. Elaiyappillai Elanthamilan et al, Strontium hexaferrite microspheres: Synthesis, characterization and visible-light-driven photocatalytic activity towards the degradation of methylene blue, *Optical Materials*, **137**, 113565**,** https://doi.org/10.1016/j.optmat.2023.113565 **(2023)**

5. Fatemeh Bavarsiha, Masoud Rajabi and Mehdi Montazeri-Pour, Synthesis of $SrFe_{12}O_{19}/SiO_2/TiO_2$ composites with core/shell/shell nanostructure and evaluation of their photocatalytic efficiency for degradation of methylene blue, *J Mater Sci: Mater Electron*, https://doi.org/10.1007\s10854-017-8098-5 **(2017)**

6. Guangmin Ren, Hongtao Han, Yixuan Wang, Sitong Liu, Jianyong Zhao, Xiangchao Meng and Zizhen Li, Recent Advances of Photocatalytic Application in Water Treatment: A Review, *Nano Materials*, **11(7),** 1804, https://doi.org/10.3390/nano11071804 **(2021)**

7. Kareema M.A., Belloa I.T., Shittua H.A., Shivaprakash P., Adedokuna O. and Arumugamd S., Synthesis, characterization and photocatalytic application of silver-doped zinc oxide nanoparticles, *Cleaner Materials*, https:\doi.org\10.1016\ j.clema.2022.100041 **(2022)**

8. Kumari Harita et al, A Review on Photocatalysis Used for Wastewater Treatment: Dye Degradation, *Water Air Soil Pollut* **234**, 349, https://doi.org/10.1007/s11270-023-06359-9 **(2023)**

9. Lázaro Nascimento Ribas, Bulhoes L. and William Leonardo da Silva, Study of the Photocatalytic Activity Using Silica-Based Materials Doped with Silver Nanoparticles for Degradation of Rhodamine B Dye, *Water Air and Soil Pollution*, **231**, https://doi.org/10.1007/s11270-020-04553-7 **(2020)**

10. Mustapha S., Tijani J.O., Ndamitso M.M., Abdulkareem A.S., Shuaib D.T., Amigun A.T. and Abubakar H.L., Facile synthesis and characterization of TiO_2 nanoparticles: X-ray peak profile analysis using Williamson–Hall and Debye–Scherrer methods, *International Nano Letters*, https://doi.org/10.1007/s40089-021-00338-w **(2021)**

11. Raba'ah Syahidah Azis, Sakinah Sulaiman, Idza Riati Ibraim, Azmi Zakaria, Jumiah Hassan, Nor Nadhirah Che Muda, Rodziah Nazlan, Norlaily M. Saiden, Yap Wing Fen, Muhammad Syazwan Mustaffa and Khamirul Amin Matori, Influence of pH Adjustment Parameter for Sol-Gel Modification on Structural, Microstructure and Magnetic Properties of Nanocrystalline Strontium Ferrite, *Nanoscale Research Letters*, https://doi.org/10.1186/s11671-018-2562-x **(2018)**

12. Sarachchandra Naraginti, Thejaswini T.V.L., Prabhakaran A., Sivakumar, Satyanarayana V.S.V. and Arunprasad A.S., Enhanced photocatalytic activity of Sr and Ag co-doped TiO_2 nanoparticles for the degradation of Direct Green-6 and Reactive Blue-160 under UV & visible light, *Spectrochemical Acta Part A: Molecular and Biomolecular Spectroscopy*, **149**, 571, http://dx.doi.org/10.1016/j.saa.2015.04.101 **(2015)**

13. Somasekhar Ryali and Paul Douglas Sanasi, Graphene oxide–nano-titania composites for efficient photocatalytic degradation of indigo carmine, *Journal of the Chinese Chemical Society*, **65**, 1423, https://doi.org/10.1002/jccs.201800154 **(2018)**

14. Tejashwini D.M. et al, Nano ferrites in photocatalytic wastewater treatment: Advancements, characterization and environmental implications, *Results in Chemistry*, **7**, 101247, https://doi.org/10.1016/j.rechem.2023.101247 **(2024)**

15. Thuy Thi Thanh Le and Trinh Dinh Tran, Photocatalytic Degradation of Rhodamine B by C and N Codoped TiO_2

Nanoparticles under Visible-Light Irradiation, *Hindawi Journal of Chemistry*, https://doi.org/10.1155/2020/4310513 **(2020)**

16. Wei Chen, Qingyun Liu, Xixi Zhu and Min Fu, One-step in situ synthesis of strontium ferrites and strontium ferrites/graphene composites as microwave absorbing materials, *RSC Adv.*, **7**, 40650, https://doi.org/10.1039/c7ra05700h **(2017)**

17. Xinyu Gao and Xiangchao Meng, Photocatalysis for Heavy Metal Treatment, *Processes*, **9(10)**, 1729, https://doi.org/ 10.3390/pr9101729 **(2021)**

18. Zi Z.F., Sun Y.P., Zhu X.B., Yang Z.R., Yang Z.R. and Song W.H., Structural and magnetic properties of $SrFe_{12}O_{19}$ hexaferrite synthesized by a modified chemical co-precipitation method, *Journal of Magnetism and Magnetic Materials*, https://doi.org/10.1016/j.jmmm.2008.06.0091 **(2008)**.

(Received 17th September 2024, accepted 20th November 2024)